Carbonate reservoir quality and permoporosity obliteration due to silicification processes in the Barra Velha Formation, Santos Basin, Southeastern Brazil

Igor Lima de Jesus[1]* (ID), Francisco Romeiro Abrantes Jr.[1,2] (ID), Danilo Jotta Ariza Ferreira[3] (ID), Wagner Moreira Lupinacci[1,2] (ID)

Abstract

Silicification is a diagenetic process commonly observed in sedimentary sections of the Aptian carbonate deposits of the Santos Basin that involves the replacement of carbonate minerals with silica. It is mostly associated with hydrothermal fluids percolating through faults and fractures. CO_2 degassing favors an increase in acidity. Consequently, the fluids became subsaturated with calcite and supersaturated with silica. Given the increase in silica content, two distinct behaviors were identified: reduction and enhancement of permoporous properties. The aim of this work is to identify permoporous alteration due to silicification in the Barra Velha Formation. To accomplish this, a qualitative analysis was conducted correlating acoustic borehole images, nuclear magnetic resonance porosity and permeability, and elemental capture spectroscopy logs were performed, followed by a quantitative analysis based on crossplot evaluation. The Barra Velha Formation was divided into three intervals with respect to silica content. The common behavior observed is permoporosity reduction associated with silica increase, but locally, permoporosity enhancement associated with silica increase was also identified. Finally, we established a direct relationship between calcite dissolution and silica precipitation, a well-defined trend characterized by sonic log (DT) reduction and density increase, and an inverse relationship between acoustic impedance and permoporous properties. Finally, the quantitative analysis also favored improving the lack of reservoir qualities of the intrusive igneous interval.

KEYWORDS: silicification; permoporous properties; acoustic borehole image; elemental spectroscopy; Santos Basin.

INTRODUCTION

Silicification of carbonate rocks involves the replacement of carbonate by silica (SiO_4-opal and quartz) as well as the precipitation of pore-filling silica cement (Tucker and Wright 1990, Flügel 2010, Butts 2014). Bustillo *et al.* (2002) and Bustillo (2010) suggest that silicification is a significant diagenetic phenomenon of ancient carbonate rocks that may illuminate diagenetic aspects of the carbonate host rock's diagenetic history (Armenteros 2010, Lima and De Ros 2019, Menezes *et al.* 2019).

The task of predicting silica sources is quite challenging due to the variety of formation mechanisms not fully understood or constrained for the ancient lacustrine systems (Bustillo 2010, Fernández-Ibánez *et al.* 2022). This diagenetic process

has been widely studied recently, identifying different silica sources that contributed to the silicification process (Herlinger *et al.* 2017, Lima and De Ros 2019, Sartorato *et al.* 2020, De Ros 2021, Basso *et al.* 2022, Fernández-Ibánez *et al.* 2022).

Even though it is not completely understood, apparently there is a consensus among different authors about the major sources of silica in sediments.

I. Changes in lake water chemistry. Due to climatic variation, an increase in water input may reduce lake water pH, favoring Mg-clay destabilization and releasing SiO_2 into the solution. Consequently, water becomes supersaturated with silica, leading to precipitation (Hesse 1989, Flügel 2010, Tosca and Wright 2018, Wright and Barnett 2020, Gomes *et al.* 2020, Sartorato *et al.* 2020, De Ros 2021, Fernández-Ibánez *et al.* 2022);

II. Redistribution of biogenic silica due to its higher susceptibility to dissolution, commonly observed as diatoms and cyanobacteria (Hesse 1989, Bustillo 2010, Flügel 2010, De Boever *et al.* 2017, Sartorato *et al.* 2020, Fernández-Ibánez *et al.* 2022). Although there is no direct evidence of diatoms in pre-salt carbonates, cyanobacteria have been identified to deposit silica on extracellular polymeric substances (EPS) and may be hypothesized as a potential source of silica (Fernández-Ibánez *et al.* 2022);

III. Silica supplied in solution by hydrothermal fluids from magmatism is brought to the lake waters *via* faults and

[1]Exploratory Interpretation and Reservoir Characterization Group, Department of Geology and Geophysics, Universidade Federal Fluminense – Niterói (RJ), Brazil. E-mails: igor_lima@id.uff.br; fabrantes@id.uff.br; wagnerlupinacci@id.uff.br

[2]National Institute of Science and Technology of Petroleum Geophysics – Niterói (RJ), Brazil.

[3]Schlumberger Brazil Research and Geoengineering Center – Rio de Janeiro (RJ), Brazil. E-mail: dferreira8@slb.com

*Corresponding author.

fractures (Mercedes-Martín *et al.* 2019, Wright 2020, Fernández-Ibáñez *et al.* 2022). The warmer waters with silica solubility and associated higher concentrations of silica interact with the lake waters, and silica may become strongly supersaturated, which favors its precipitation (Hesse 1989, Bustillo 2010, Pinto *et al.* 2017, Lima and De Ros 2019, Sartorato *et al.* 2020, Wright and Barnett 2020, De Ros 2021, Fernández-Ibáñez *et al.* 2022).

The heterogeneity of Aptian carbonate reservoirs from Brazil's pre-salt is commonly associated with their geological complexity, which makes oil and gas production quite challenging (Farias *et al.* 2019, Gomes *et al.* 2020, Ferreira *et al.* 2021). Therefore, understanding diagenetic processes, such as silicification, becomes relevant for identifying their impact on reservoir characterization.

Silicification of carbonate sediments can apparently occur at different stages of their diagenetic evolution. The carbonate rocks affected by silicification and dissolution processes may have permeability and porosity enhanced or reduced (Moore 1989, Ahr 2008, Flügel 2010). In general, the replacement of limestone by silica can actually reduce porosity due to cementation rather than enhance it. Porosity enhancement is largely associated with dissolution and may occur associated with silicification (Ahr 2008, Sartorato *et al.* 2020, De Ros 2021).

The dissolution of Mg-clays matrix generated an important proportion of the present porosity of pre-salt reservoirs (Sartorato *et al.* 2020, Wright and Barnett 2020, De Ros 2021, Wright 2020, Fernández-Ibánez *et al.* 2022). The circulation of fluids during burial was focused through levels with abundant secondary porosity, or preserved primary porosity, and through faults and fracture zones. The flow of hydrothermal fluids through these structures promoted significant dissolution and porosity enhancement in several areas but also strong porosity reduction in other places through the precipitation of quartz, chalcedony, dolomite, and pyrite (Lima and De Ros 2019, De Ros 2021).

Since there are several possibilities and uncertainties related to silicification processes in pre-salt reservoirs and their impacts on their petrophysical reservoir properties, the objective of this study is to identify and infer the silica volume influence to enhance or reduce permoporosity and characterize the silica volume impact on different reservoir properties for pre-salt reservoirs. To perform this evaluation, we analyzed qualitatively and quantitatively several well logs, including image borehole logs, and core information from two wells located in a pre-salt field from the Santos Basin within the Barra Velha Formation.

GEOLOGICAL SETTINGS

The Santos Basin is a passive margin sedimentary basin located on the southeast margin of Brazil. It is limited to Pelotas Basin, in the south, bounded by Florianopolis High, and to the north by Campos Basin, bounded by Cabo Frio High (Fig. 1). The basin covers a total area of approximately 350.000 Km^2 and extends between parallels 23º and 28º South, along the coast of Santa Catarina, Paraná, São Paulo, and Rio de Janeiro Brazilian states (Moreira *et al.* 2007).

This basin was formed during the rupture of the supercontinent Gondwana between the Late Jurassic and Early Cretaceous ages. Its formation was characterized by extensional tectonic efforts that subsequently developed the Atlantic Ocean and caused the separation of the South American and African continents (Moreira *et al.* 2007). According to the authors, basin tectonic evolution is divided into three sedimentary super sequences: rift, post-rift, and drift. The basement of Santos Basin is characterized by granites and gneisses from the Precambrian age and Neoproterozoic metasediments of the Ribeira Belt (Moreira *et al.* 2007).

The pre-salt interval encompasses the rift (Camboriu, Piçarras, Itapema, and Lower Barra Velha formations) and post-rift phases (Upper Barra Velha Formation). The rift phase is characterized by a sequence of tectonic events that generated the Gondwana supercontinent's fragmentation through continental crust stretching and thinning processes during the Lower Cretaceous (Muniz and Bosence 2015). Mohriak *et al.* (2008) point out the space-forming mechanism for sedimentary accommodation and widespread normal fault generation as a consequence of the mechanical subsidence process. The rift structures present a NE-SW orientation, following the previous basement structural behavior, represented by faults limiting horsts and grabens (Szatmari and Milani 2016, Stanton *et al.* 2014). The post-rift phase comprises sedimentary deposition from the Aptian, characterized by a reduction of tectonic activity that favored the basinal domain and conditioned a depositional quiescence identified as a sag phase (Moreira *et al.* 2007). Finally, a thick layer of marine evaporites from the Ariri Formation overlies the post-rift phase, indicating an arid climate during the Aptian and Albian ages of the Santos Basin (Moreira *et al.* 2007).

Lithostratigraphically, the Camboriú formation comprehends mafic rock intrusions and extrusions associated with Gondwana's breakup. The Piçarras formation is characterized by alluvial sediments and shales of talc-stevensitic composition (proximal and distal areas, respectively). The Itapema formation comprises bivalve bioclastic rudstones in structural highs and organic-rich shales in distal basin portions (Moreira *et al.* 2007). The Barra Velha Formation (BVF) is characterized by reworked and *in situ* limestones, of which the latter present controversies related to their origin. Some authors point to a biotic genesis (Moreira *et al.* 2007, Carminatti *et al.* 2009, Terra *et al.* 2010, Kattah 2017), while others indicate a more chemically controlled origin (Wright and Barnett 2015, 2020, Farias *et al.* 2019, Gomes *et al.* 2020, Wright 2020, De Ros 2021, Carvalho *et al.* 2022). The Ariri Formation capes the post-rift, and it is composed mostly of halite and anhydrite, but also of tachyhydrite, carnallite, and sylvinite (Moreira *et al.* 2007).

In opposition to the supersequence limits proposed by Moreira *et al.* (2007), Wright and Barnett (2015) suggested that the lower portion of the Barra Velha Formation (BVF) is partially contained in the rift phase instead of within the sag phase due to tectonic differences observed in the lower and upper portions. This updated interpretation has been accompanied by several authors (Buckley *et al.* 2015, Szatmari and

Milani 2016, Tosca and Wright 2018, Farias *et al.* 2019, Gomes *et al.* 2020, Ferreira *et al.* 2021). For these authors, the Intra-Alagoas unconformity is a regional surface that subdivides the BVF portions (Fig. 2).

METHODOLOGY

This study presents well log data and routine core analysis (RCAL) related to the Barra Velha Formation (BVF) from two wells drilled in a Santos Basin field, named Wells A and B (Fig. 1). The data were obtained from the National Agency of Petroleum, Natural Gas and Biofuels (ANP). The well-log evaluation was performed with the software Techlog™, and two analyses were provided. The qualitative analyses were based on well logs to identify different silica intervals and their relationship to permoporosity. For these analyses, the following well-logs were considered: gamma-ray (GR_EDTC), caliper (HCAL), acoustic impedance (P-impedance), elemental capture spectroscopy (ECS), acoustic BHI (dynamic and static), NMR effective porosity (PHIE_NMR), and permeability (PERM_NMR). Porosity and permeability logs were correlated to laboratory measurements of side-wall cores or plugs from cores, where available.

Initially, the well logs were submitted to quality control to assure the correct depth corrections due to:
I. acquisition occurring from different runs;
II. removal of spikes and artifact measurements that may compromise the formation evaluation;
III. merging of curves;
IV. interpolation of short gap intervals from different logging phases.

The final part of the QC analysis was the caliper validation for borehole stability when logging to identify compromised intervals due to washout.

The ECS logs allow the estimation of rock element concentrations based on nuclear interactions between neutrons and different atoms. Every atom has its own gamma-ray energy capture and distribution spectrum. Then, the energy spectrum is decomposed into the different elements of the formation (spectral stripping). The elemental relative yields are the product of spectral stripping. Finally, the dry weight of each element is derived from the yields, and an oxide-closure model is used to associate each element with its corresponding oxide (Herron and Herron 1990, Radtke *et al.* 2012).

The acoustic borehole image tool (BHI) has a transducer that rotates in the center of the well, performing a 360° well wall cover for the acquisition of acoustic amplitude and time-travel array logs. These image logs allow the identification of geological features, especially structural ones, and the variation of amplitude particularly assists the determination of pore space aperture. Usually, low amplitude values imply an open pore space, while high amplitude values are interpreted as a closed pore space (Gaillot *et al.* 2007). In our study, BHI logs were mainly used for the identification of porosity type and fracturing in the qualitative analysis.

For effective porosity and permeability evaluation, we used the NMR logging tool, which presents the best accuracy for *in situ* estimation (Ellis and Singer 2010). The tool excites hydrogen atom spin in the fluid inside porous space around a fixed magnetic field (Coates *et al.* 1999). The NMR raw data is associated with the amplitude of the spin echoes as a function of time. Then, the transversal relaxation decay
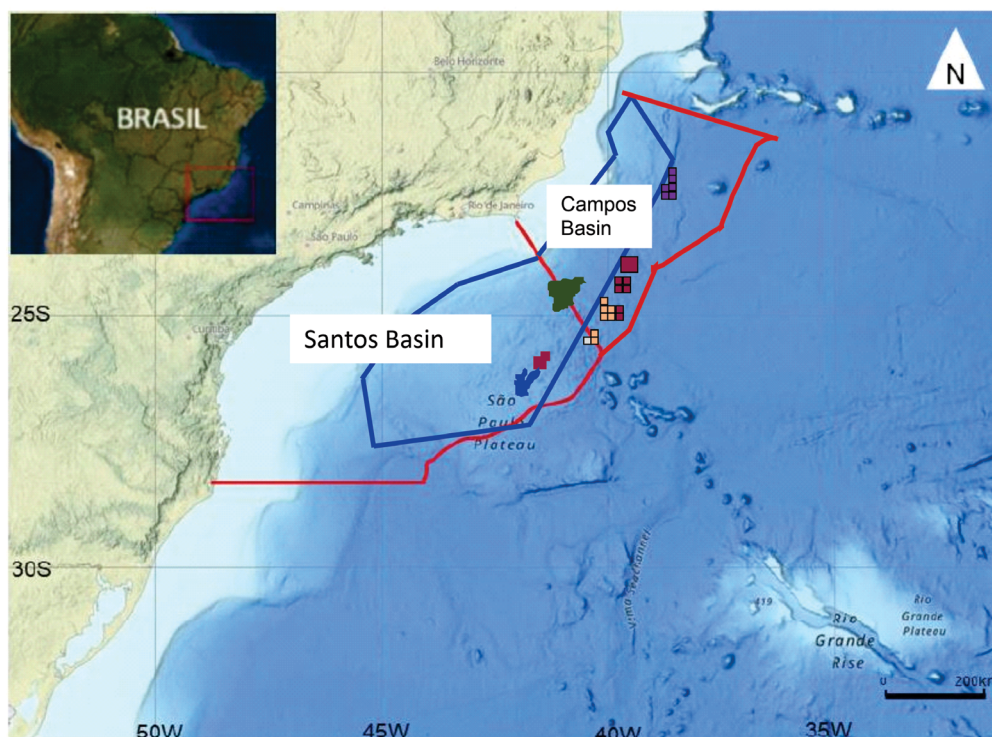
Source: De Jesus *et al.* (2021).
Figure 1. Map illustrating the location of the Santos and Campos Basins. The blue polygon indicates the pre-salt province, the colored blocks are prospects, and the irregular polygons are production fields.

Figure 2. Schematic illustration of tectono-stratigraphic evolution of the Santos Basin.

(T2) is measured through a multi-exponential model. The volume of fluid in the pore space is proportional to the number of hydrogen nuclei in the formation fluid. Each T2 is related to pore size. Therefore, NMR total porosity can be separated into three parts: clay-bound water (CBW) is characterized by a pore throat size of less than 0.3 μm, always filled with water and ineffective porosity; the bulk volume of irreducible water (BVI) has a pore throat size between 0.3 and 4 μm, and free fluids (FF) have pore throat sizes larger than 4 μm.

It is important to highlight that the presence of igneous rock affects the feasibility of some tools such as NMR and, also due to tool configuration, NMR porosity, and permeability readings may be heavily compromised by the presence of washover zones. In cases where igneous rocks are present, the use of a sonic log offers a more reliable porosity and permeability evaluation. Then, for the intrusive Well A segment, the porosity and permeability were estimated from the sonic log instead of the NMR logs. After that, NMR logs from non-igneous zones were merged with igneous zones sonic-derived logs for porosity (PHIE_MERGE) and permeability (PERM_MERGE).

Additionally, to establish a qualitative classification based on the quantitative values measured for porosity and permeability logs, five ranks of reservoir quality were created, as illustrated in Table 1.

Finally, by aiming to characterize different reservoir properties, quantitative analyses were performed through curve crossplots evaluation applied individually for both wells: calcite volume *vs.* silica volume; sonic slowness *vs.* density; P-impedance *vs.* silica volume.

RESULTS

Qualitative analysis of permoporosity in the Barra Velha Formation

Based on visual analysis and interpretations of well logs, different patterns and log signatures were identified for the wells used in this study (Figs. 3 and 4). In a general view, a homogeneous behavior was observed in the wells:

I. low GR values and a continuous caliper;
II. p-impedance also presents low values (between 12 and 15 MPa.m/s), but increases upward;
III. permoporosity decreases upward;
IV. volumes of calcite and silica seem to present a complementary behavior.

The silica volume shows a well-defined gradual increase upward, while the calcite volume decreases upward. The formation was divided into three intervals according to silica volume behavior, namely, S3, S2, and S1 (from bottom to top). The uppermost portion of this succession is characterized by an intrusive igneous interval. Along the whole formation, it can be observed that an improvement of permoporous properties is associated with silica volume deterioration. The main difference between the wells used in the study is the presence of an intrusive igneous interval in the upper portion of Well A. It is important to highlight that no igneous body was observed in Well B.

Silica Interval 3

The interval is 12 m in Well A (X115/127 m) and 67.6 m (X125.40/X193 m) in Well B. Both wells are characterized by limestone. Some of the limestones are described as shrubs and spherulites (in Well B). The log signatures are quite similar for both wells: very low GR values (with some spikes in Well B), a slight upward increase in acoustic impedance, and the lowest silica content average registered for the whole formation (4.53 and 11.49%, respectively, for Wells A and B). On the contrary, this interval shows a higher average for porosity (12.54 and 13.85%, respectively, for Wells A and B) and permeability (96.86 and 229.68 mD, respectively, for Wells A and B). In this interval, porosity varies from good (10–15%) to very good (15–20%), and sparse excellent values (20–25%) in Well B. It is important to observe that permeability goes along with the same variation:

Table 1. Qualitative classification criteria based on porosity and permeability well log values.

Porosity Range (%)	Permeability Range (mD)	Qualitative Description	Colors Used in Figures
0–5	0.1–1	Low	
5–10	1–10	Moderate	
10–15	10–100	Good	
15–20	100–1000	Very Good	
20–25	1000–10000	Excellent	

good (10–100 mD) to very good (100–1,000 mD) and sparse excellent values (1,000–10,000 mD) for Well B.

When comparing porosity and permeability to silica content, it is possible to observe an increase of the latter and a reduction of the former but there is an exception, locally noticed in depths X157 and X148 m (Well B), which is the increase of silica content correlated to porosity and permeability enhancement. Apparently, the proportion of silica precipitation is lower than that of calcite dissolution, favoring porosity, and permeability enhancement.
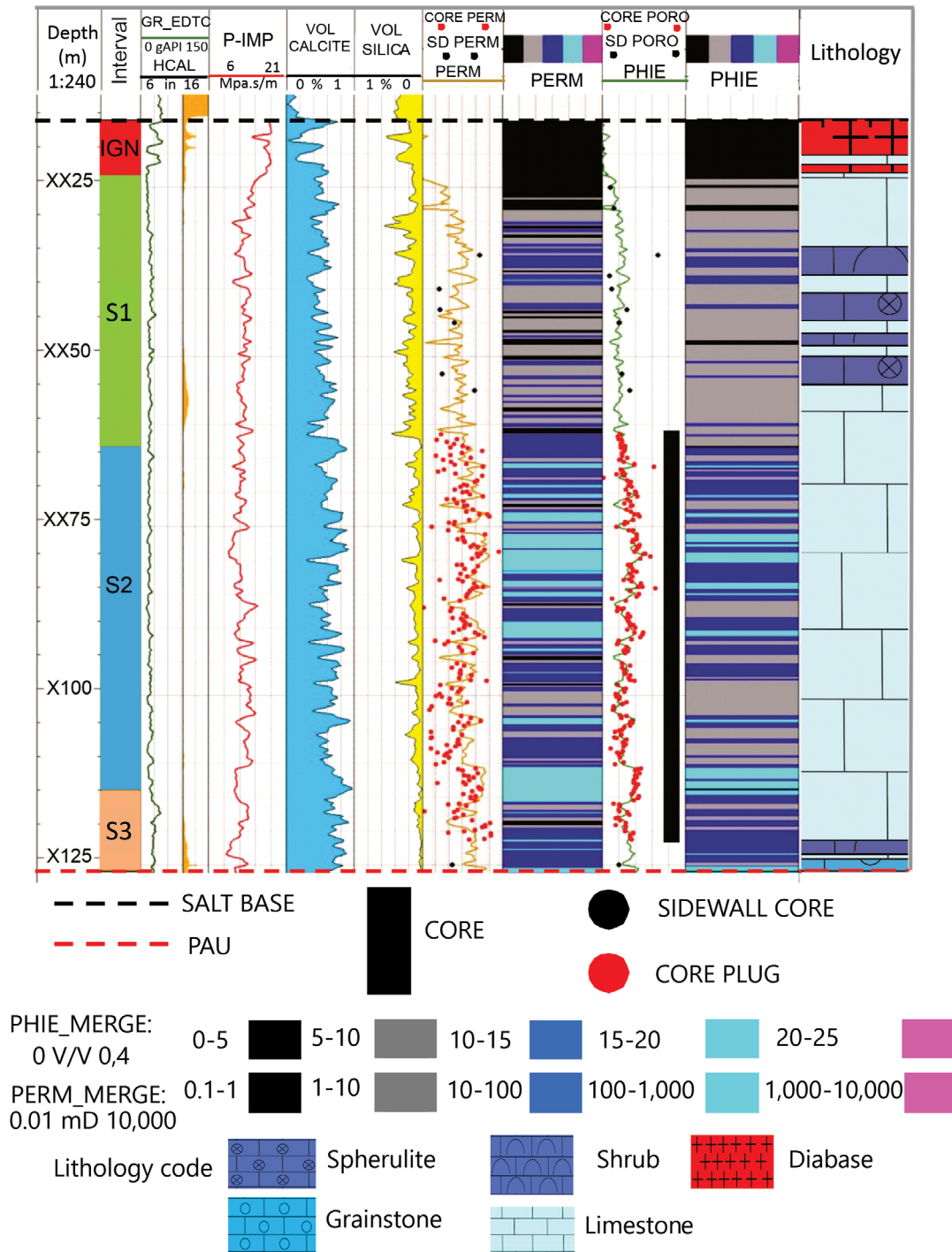

Figure 3. Well log analysis of the BVF in the Well A. Tracks: (1) TVDSS; (2) Silica intervals; (3) Caliper (HCAL) (orange), Gamma-ray (GR_EDTC) (green); (4) P-impedance (red); (5) Calcite volume (VOL_CALCITE) (blue); (6) Silica volume (VOL_SILICA) (yellow); (7) Merged permeability (PERM_MERGE) (orange); (8) Permeability classes; (9) Merged porosity (PHIE_MERGE) (green); (10) Porosity classes; and (11) Lithology. Dashed lines indicate Pre-Alagoas unconformity (red) and salt base (black).

Silica Interval 2

The interval displays 37.40 m in Well B (XX88/XX125.40 m) and 51 m (XX64/X115 m) in Well A. In both wells, lithology is described as limestone. The log signatures are characterized by lower GR values, compared to the interval S3 and present steady behavior. The acoustic impedance shows spiky behavior but without high values variations. The silica volume presents a higher average (10.63 and 12.96%, respectively, for Wells A and B) compared to interval S3. The porosity varies in both wells from moderate (5–10%) to good (10–15%) and some minor very good (15–20%), while permeability is mostly characterized by
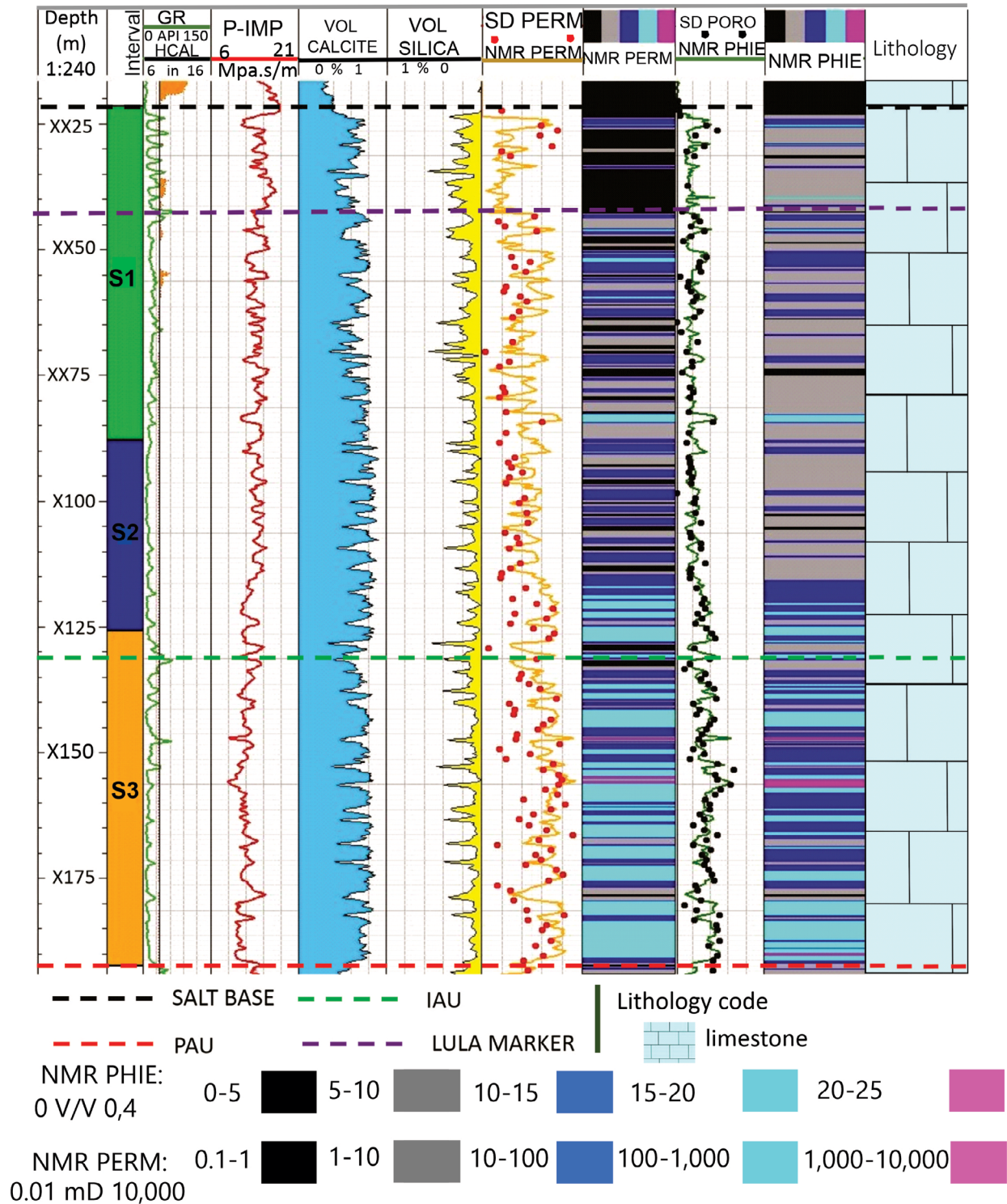

Figure 4. Well log analysis of the BVF in the Well B. Tracks: (1) TVDSS; (2) Silica intervals; (3) Caliper (HCAL) (orange), Gamma-ray (GR_EDTC) (green); (4) P-impedance (red); (5) Calcite volume (VOL_CALCITE) (blue); (6) Silica volume (VOL_SILICA) (yellow); (7) Permeability from NMR (NMR_PERM) (orange); (8) Permeability classes; (9) Porosity from NMR (PHIE_NMR) (green); (10) Porosity classes; and (11) Lithology. Dashed lines indicate unconformities: Pre-Alagoas (red), Intra-Alagoas (green), Salt Base (black), and Lula Marker (purple).

good (10–100 mD), very good (100–1,000 mD), and sparse moderate (1–10 mD).

It is worthy of notice that the porosity averages are lower in interval S2 for both wells (11.61 and 9.52%, respectively) compared to interval S3, while the permeability average is lower for Well B (42.55 mD) and higher (124.79 mD) for Well A, compared to the interval S3. Although there is a regular trend of silica content increase associated with porosity reduction, it is possible to observe an increase in silica and porosity enhancement at depth X163.4 m of Well B and depth XX85 m of Well A. The higher average of permeability in interval S2, compared to interval S3 occurs due to dissolution that favors fluid flow, increasing permeability (XX67 m, XX71.60 m, XX74 m, and XX81 m). This behavior is more clearly evidenced through BHI borehole image analysis.

Silica Interval 1

The interval displays 39.9 m in Well A (X24.90/X64.80 m) and 66 m (X22/XX88 m) in Well B. The lithology is mostly described as limestone except for some shrubs and spherulites observed in Well A. The GR values are very low in both wells, while the acoustic impedance increases upward in Well A and shows spiky behavior but without high-value variations in Well B. The silica volume is evidently higher than in intervals S3 and S2. The value difference indicating higher silica content can be confirmed through average observation (20.14% in Well A and 18.21% in Well B, respectively).

The porosity varies in both wells from moderate (5–10%) to good (10–15%), while the permeability varies in both wells from moderate (1–10 mD) to good (10–100 mD), but it can be also observed sparse low values (0.01–1 mD). The porosity and permeability averages confirm quantitatively the observed reduction (8.03 and 8.22%, respectively, for Wells A and B) and (8.84 mD and 23.24 mD, respectively, for Wells A and B).

In the upper portion of Well B, a particular pulsed feature is characterized by nine peaks in a row, known as the Lula Marker (Wright and Barnett 2020), between XX24 m and XX43 m; Fig. 4). This feature is a regional marker, indicative of a very shallow lake with a large extension, and it is observed in several logs from different fields in Santos Basin (Wright and Barnett 2020). Apparently, due to the intrusive igneous interval that capes BVF in well B, this feature was not recognized.

Intrusive igneous interval

The intrusive igneous interval (XX16/XX24.90 m) in the upper portion of Well A shows permoporosity values close to zero (Fig. 3). It is important to highlight that the ~10 m carbonate rocks (S1) immediately below the igneous rock present an accentuated reduction of permoporous properties, probably due to contact metamorphism.

Calcareous framework and silica distribution

Figures 5, 6, and 7 show the relationship between acoustic BHI and silica volume for segments of wells A and B. The dark colors of dynamic and static acoustic BHI (ubi_amp_dyn and ubi_amp_stat) correspond to low amplitude values interpreted to be open pore space, while bright colors are associated with

high amplitude, interpreted to be silicified layers (Lai *et al.* 2018, Fernández-Ibánez *et al.* 2022).

Based on BHI interpretation, the silicified layers are characterized as homogeneous, bright, massive portions with high amplitude and a very low roughness texture. It also observed a lack of internal bedding or structures and low visual porosity similar to acoustic image log facies (AIF3), as defined by Basso *et al.* (2022). In interval S2 of Well B, the silica layers present a few discrete fractures and geometric structures with the same orientation, interpreted as breakouts.

Intercalated with silicified layers, another image log pattern was identified, which is characterized by low amplitude values, very high roughness texture, and irregular bedding, similar to AIF2 (Basso *et al.* 2022). Eventually, bright patches of different geometries and sizes are observed (Lai *et al.* 2018), which may indicate irregular silicification or intraclast grains. The high roughness can be associated with open pore space, indicating millimetric or centimetric-size interconnected vugs.

The observed patterns for silicified layers and pore spaces can be seen in all three intervals. It is worth mentioning that the silicified layers identified in BHI can be fairly correlated to the silica volume well log increase for both wells. The silica usually occurs as continuous bed layers with thicknesses ranging from 1 to tens of centimeters. These silica layers tend to occur plane-parallel and concordantly with adjacent limestone bedding. According to Fernández-Ibánez *et al.* (2022), the conformity of silicified layers to adjacent limestone strata can be interpreted as a replacement phase (Fig. 5A).

The silica layer boundaries are observed as irregular (X109.40 m; Fig. 6C) or sharp contacts (XX85 m; Fig. 5C) with limestone adjacent strata. Several silica intraclasts are observed above and sometimes below the silica layers (Fig. 5C). In interval S2 of both wells, there is a well-defined intercalation of silica layers and limestones with vuggy porosity. Although vugs are observed in several parts of all three intervals, along the whole formation, interval S1 of Well A exemplifies a high centimetric-size vug density, which reaches moderate porosity (5–10%) and moderate (1–10 mD) to good (10–100 mD) permeability values (XX56.30/XX58.50; Fig. 5B). It is important to highlight that vugs are the product of dissolution, which favors porosity enhancement, while silica intraclasts may be a product of irregular silicification or rework processes. Also, the anomalous permoporosity enhancement behavior associated with silica volume increase can be observed at XX85 m (Fig. 5C).

Figures 6 and 7 show two different segments in Well B that illustrate two different permoporosity behaviors associated with silica volume increase:

I. the silica volume increase is associated with permoporous reduction (Fig. 6);
II. the silica volume increase is associated with permoporosity enhancement (Fig. 7).

In both segments, a series of well-defined intercalations of permoporosity reduction and enhancement are observed.

The segments displayed in Figs. 5B, 5C and 7 illustrate the anomalous permoporosity enhancement behavior related to the

silica volume increase presented in both wells. The interpretation of the BHI allowed the identification of silica layers with fracture and dissolution features, which were not observed in the segment with the opposite behavior. The action of fracturing and dissolution processes in the same strata, as a product of silicification, apparently favored permoporosity enhancement at depths X153 and X156.5 m (Fig. 7A). To highlight different features from the BHI, a 4-m interval was zoomed in the lower portion of the interval S3, between X160.9 and X164.1 m (Fig. 7B). It is noteworthy that well-defined intercalation of decimeters of plane bedding from X164 up to X162.6

m occurs (Fig. 7B). Then, it changes to intercalation of laminations up to X161 m. At depth X163.20 m, the dissolution effect to enhance pores is illustrated, as is their interconnection to favor permeability.

Finally, for a better understanding and data comparison, Table 2 summarizes the arithmetic mean and median values of the main well logs used in this work for the silica intervals in both wells. The table favors the identification of silica and permoporous property variations. Again, it is important to highlight that both wells present a general trend of decreasing permoporosity properties upwards, and consequently the
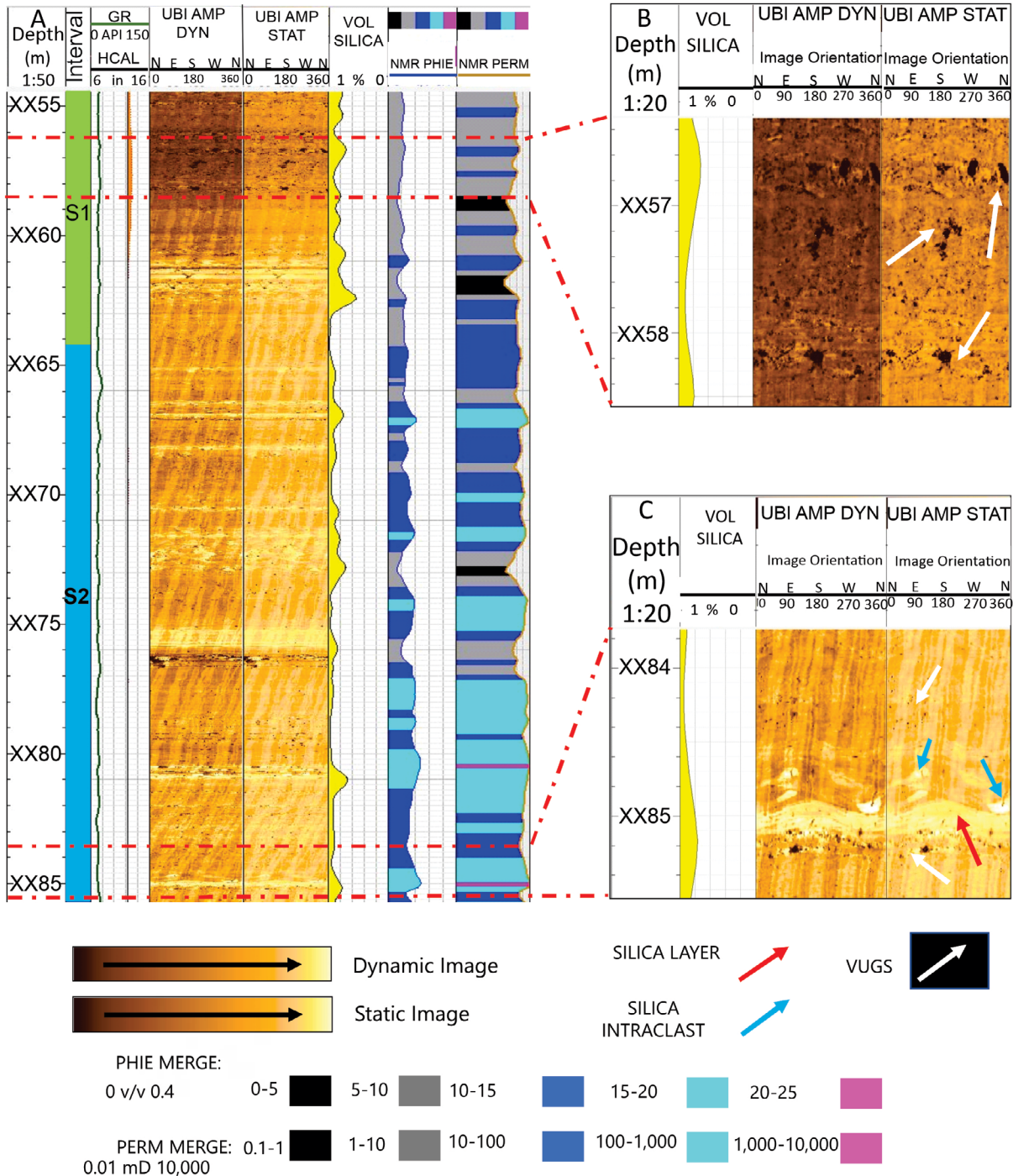

Figure 5. (A) Segment of the BVF in the Well A. Tracks: (1) TVDSS; (2) Silica Zonation; (3) Caliper (HCAL) (orange), Gamma-ray (GR_EDTC) (green); (4) Acoustic dynamic image (UBI_AMP_DYN); (5) Acoustic static image (UBI_AMP_STAT); (6) Silica intervals (VOL_SILICA) (yellow); and (7) Merged permeability (PERM_MERGE); 8-Merged porosity. (B) Intervals XX56.30/XX58.50 m. (C) XX83.75/XX85.50 m are detailed to favor features identification. White arrows indicate vugs, red arrows indicate silica layers, blue arrows indicate silica intraclasts, and green arrow indicates open fracture.

quality of reservoir properties is correlated with silica increase and calcite reduction.

Quantitative evaluation of permoporosity in the Barra Velha Formation

The quantitative analysis of the studied carbonate reservoir was built using crossplots according to petrophysical parameters estimated and available from well logs. Crossplot use favors the characterization of reservoir property variations due to silicification impact and other diagenetic processes. In this study, we use the following crossplots (Figs. 8, 9, and 10):

I. calcite volume *vs.* silica volume;
II. sonic slowness *vs.* density;
III. P-impedance *vs.* silica volume.

Calcite volume vs. silica volume

The calcite volume *vs.* silica volume crossplot performed for Well A indicates that when silica volume increases, calcite volume decreases (Figs. 8A, 8B, and 8C). From intervals S3 to S1, the silica content gradually increases upward, allowing the separation of these intervals in different zones in the silica/calcite crossplot (Fig. 8A). The intrusive igneous interval is characterized by low calcite and high silica values (Fig. 8A).
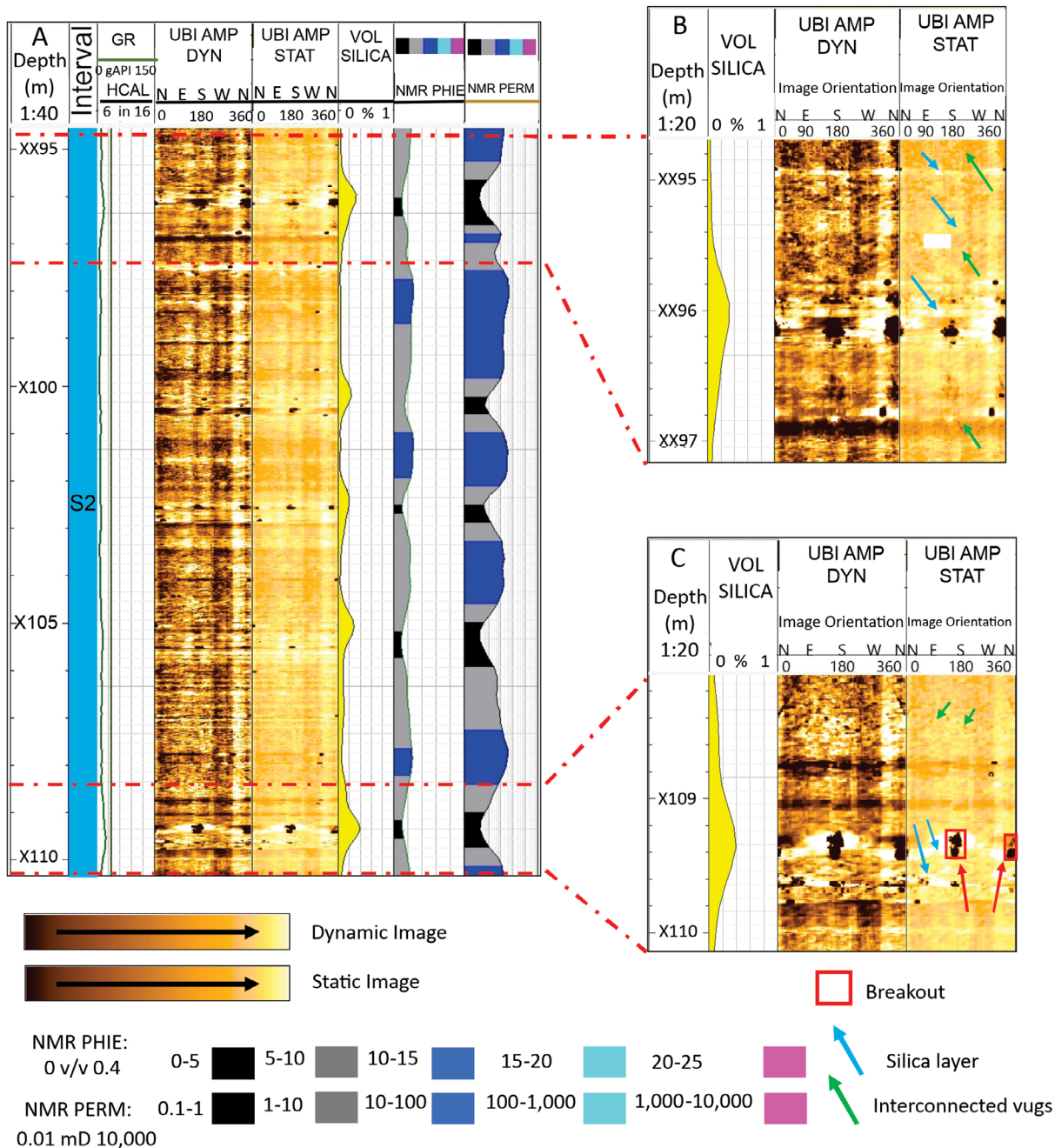

Figure 6. (A) Segment of the BVF in the Well B exhibiting levels with high-silica content and permoporosity reduction. Tracks: (1) TVDSS; (2) Silica intervals; (3) Caliper (HCAL) (orange), Gamma-ray (GR_EDTC) (green); (4) Acoustic dynamic image (UBI_AMP_DYN); (5) Acoustic static image (UBI_AMP_STAT); (6) Silica volume (VOL_SILICA) (yellow); (7) Porosity from NMR (PHIE_NMR); and (8) Permeability from NMR (NMR_PERM). (B) Intervals XX94.70/XX97.10m. (C) X108.10/X110.10 m are zoomed to favor features identification. Red rectangles indicate breakouts, blue arrows indicate silica layers, and green arrows indicate centimetric vugs.

The porosity and permeability behavior presents an opposite trend of silicification (Figs. 8B and 8C): interval S3 is mostly characterized by good to very good porosity and permeability; interval S2 has good porosity and permeability; and interval S1 presents low to moderate porosity and permeability, with minor very good values. It is noteworthy that intrusive igneous presents tightened permoporosity behavior characterized by low values.

In Well B (Figs. 8D, 8E, and 8F), a behavior similar to Well A is observed; calcite volume decreases when silica volume
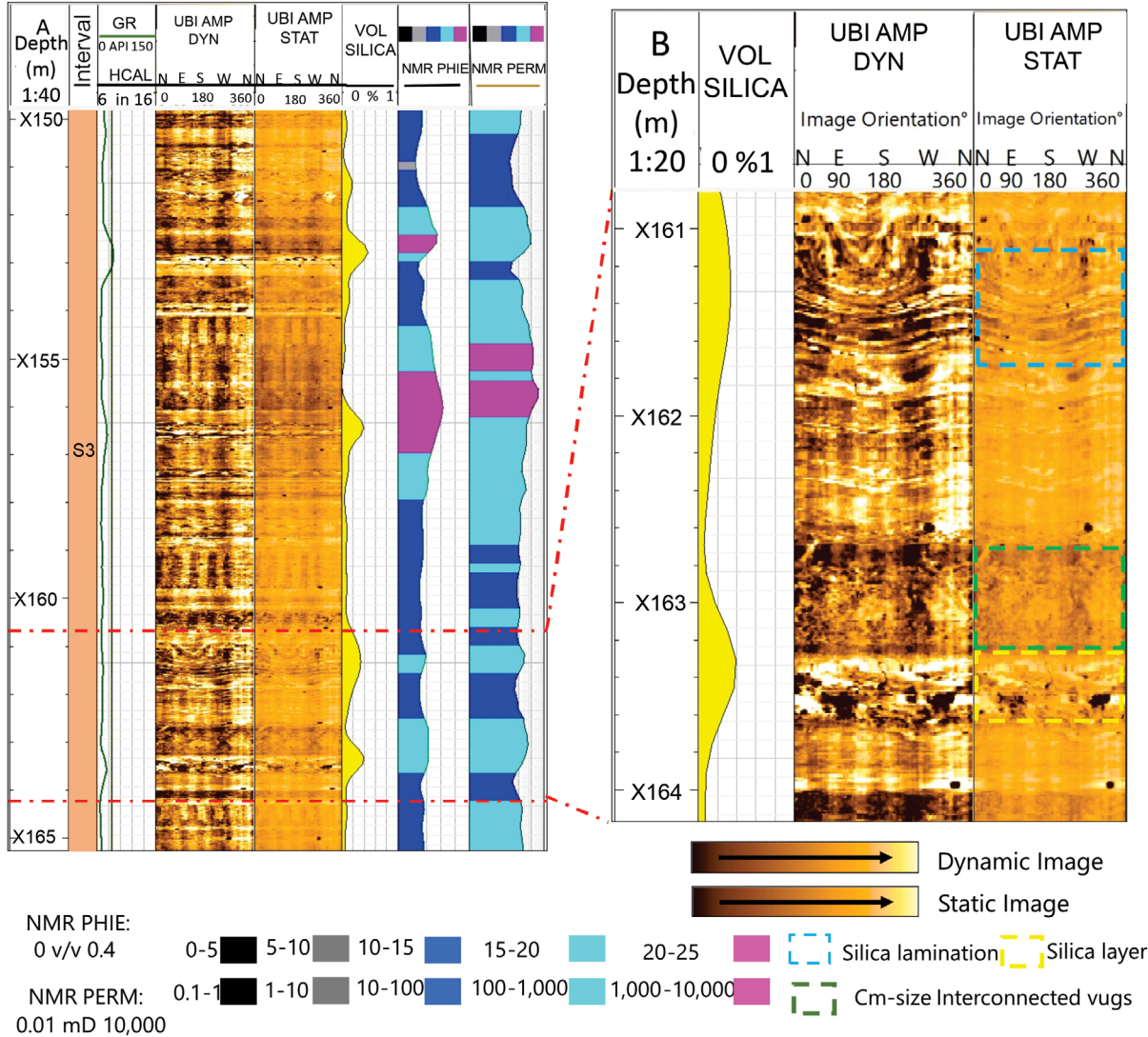

Figure 7. (A) Segment of the BVF in the Well B exhibiting levels with high-silica content and permoporosity enhancement. Tracks: (1) TVDSS; (2) Silica intervals; (3) Caliper (HCAL) (orange), Gamma-ray (GR_EDTC) (green); (4) Acoustic dynamic image (UBI_AMP_DYN); (5) Acoustic static image (UBI_AMP_STAT); (6) Silica volume (VOL_SILICA) (yellow); (7) Porosity from NMR (PHIE_NMR); and (8) Permeability from NMR (NMR_PERM). (B) Interval X160.9/X164.1 is zoomed to favor features identification. Yellow squares indicate silicified fracture layer, green squares indicate centimetric-size interconnected vugs interval, and blue squares indicate silica fractured laminations interval.

Table 2. Table with arithmetic mean and median of the main well-logs used for this work.

Well	Interval	Phie (V/V)		Perm (mD)		GR (gAPI)		Acoustic Impedance (MPa.s/m)		Silica		Calcite	
		Average (%)	Median (%)	Average	Median	Average	Median	Average (%)	Median (%)	Average (%)	Median (%)	Average (%)	Median (%)
A	S1	8.03	8.14	8.84	4.45	20.37	20.52	13.00	12.90	20.14	18.13	53.35	53.22
	S2	11.61	11.41	124.79	41.25	19.94	19.66	12.42	12.26	10.63	9.39	65.54	65.84
	S3	12.54	12.70	96.86	62.76	29.52	28.62	11.87	11.96	4.53	3.57	74.46	72.56
B	S1	8.22	7.60	23.24	2.06	21.91	19.68	14.70	14.21	18.21	16.45	70.79	72.61
	S2	9.52	9.48	42.55	15.39	12.53	11.90	13.50	13.55	12.96	9.79	74.62	70.97
	S3	13.85	14.19	229.68	126.50	16.77	13.30	11.91	11.80	11.49	8.75	76.63	79.73

increases. Although there is an overlap of the data from the three intervals, interval S3 concentrates lower silica volumes while interval S1 reaches higher silica values, corroborating the upward silica increase observed in qualitative well log analysis (Fig. 4). The porosity and permeability indicate an inverse trend to silica volume, such as in Well A (Figs. 8E and 8F): the interval S3 shows good to very good porosity and permeability and sparse excellent values; the interval S2 varies from good to very good porosity, but it can also be noticed an increase of low and moderate values, while permeability varies mostly from moderate to

good values. Finally, interval S1 predominantly shows moderate porosity and low-to-moderate permeability values.

The crossplot clarifies the opposite solubility relationship between calcite dissolution and silica precipitation (Bustillo 2010, Wright and Barnett 2020). In both wells, it is possible to identify a trend toward improving this direct relationship. The crossplot also corroborates that the volume of silica increases upward. Quantitatively, the silica volume is higher in interval S1 than in interval S3. Based on that, it is possible to infer that there is a higher accumulation of silica volume in the upper portions of BVF.
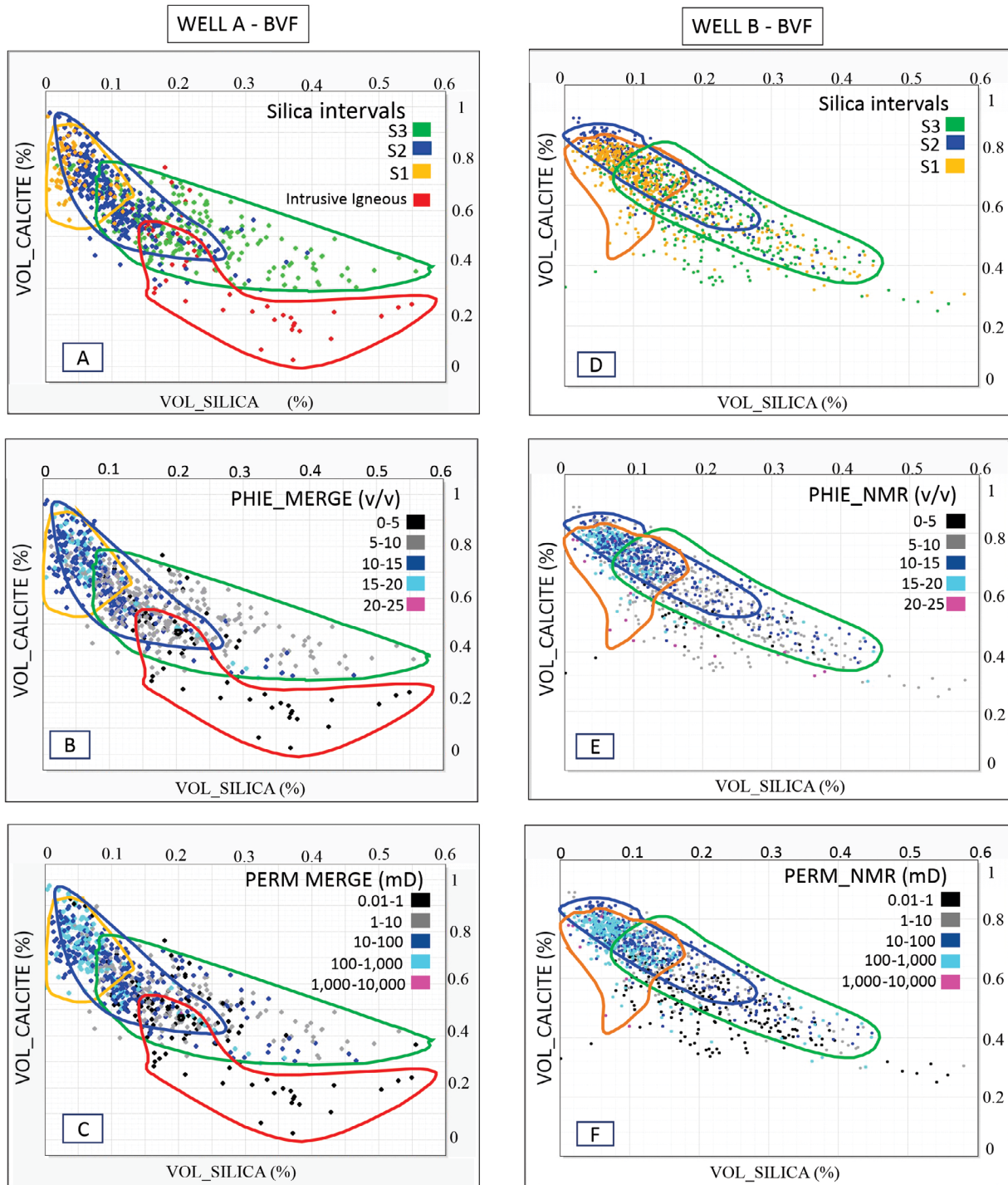

Figure 8. Crossplot of silica volume (VOL_SILICA) *vs.* calcite volume (VOL_CALCITE) for Wells A and B. (A) Silica and intrusive igneous intervals in Well A. (B) Relationship between the silica intervals, silica volume, calcite volume, and porosity characterization for Well A. (C) Relationship between the silica intervals, silica volume, calcite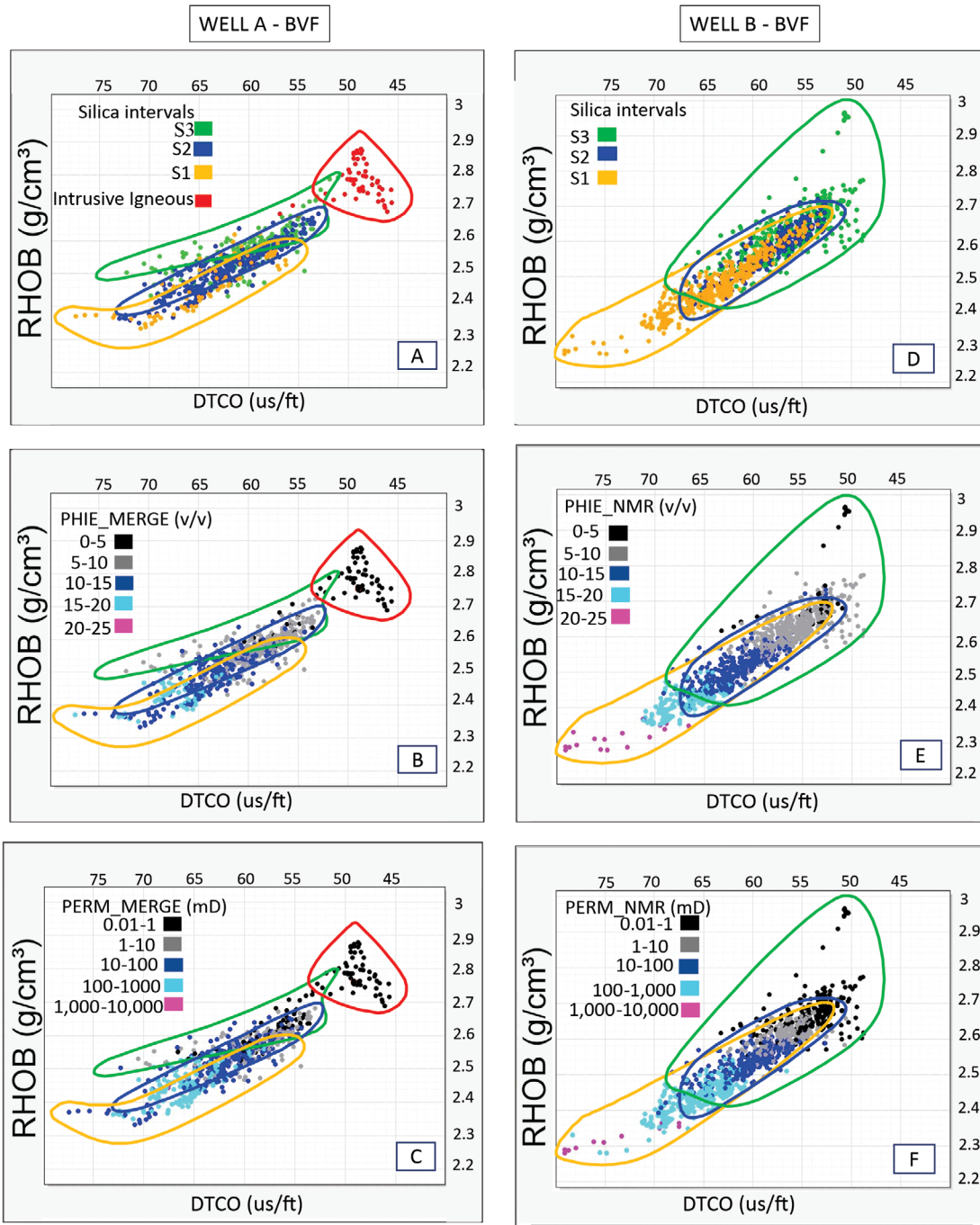 volume, and permeability characterization for Well A. (D) Silica and intrusive igneous intervals in Well B. (E) Relationship between the silica intervals, silica volume, calcite volume, and porosity characterization for Well B. (F) Relationship between the silica intervals, silica volume, calcite volume, and permeability characterization for Well B.

Figure 9. Crossplot of sonic slowness (DTCO) *vs.* density (RHOB) for Wells A and B. (A) Silica and intrusive igneous intervals in Well A. (B) Relationship between the silica intervals, DTCO, RHOB, and porosity characterization for Well A. (C) Relationship between the silica intervals, DTCO, RHOB, and permeability characterization for Well A. (D) Silica and intrusive igneous intervals in Well B. (E) Relationship between the silica intervals, DTCO, RHOB, and porosity characterization for Well B. (F) Relationship between the silica intervals, DTCO, RHOB and permeability characterization for Well B.

Sonic slowness vs. density

The sonic slowness *vs.* density crossplot presents a well-defined trend characterized by DT reduction and density increase (Figs. 9A, 9B, and 9C). The silica intervals in Well A present a slightly vertical separation according to density enhancement (Fig. 9A). The intrusive igneous interval presents higher density and lower DT values compared to silicified carbonate intervals (Fig. 8A). Interval S3 presents the best permoporosity quality, characterized by good to very good values, rarely presenting moderate values (Figs. 9B and 9C). In the S2 interval, an increase of moderate values is observed but still prevails

good to very good values of porosity and permeability (Figs. 9B and 9C). The interval S1 is characterized by moderately porosity values, but permeability seems more compromised than intervals S2 and S3. Finally, the intrusive igneous interval is characterized by low permeability and porosity values (Figs. 9B and 9C).

In Well B, a well-defined overlap of the silica intervals is registered (Figs. 9D, 9E, and 9F), but the interval S3 is represented by the lowest RHOB and highest DT values, and the interval S1 by the lowest DT and highest RHOB values (Fig. 9D). The interval S2 has an intermediate behavior (Fig. 9D).

The best permoporosity values (very good to excellent) mostly occur in the interval S3 zone, while interval S1 presents predominantly low to moderate values (Figs. 9E and 9F). The interval S2 is characterized by intermediate permoporosity values (moderate to good) that also include the lower interval S3 values and the higher interval S1 values (Figs. 9E and 9F). It is also important to highlight that permoporosity displays well-defined boundaries from low to excellent values, favoring its separation (Figs. 8E and 9F).

Based on the crossplot interpretation, it is possible to infer that the upward increase in silica content may directly impact density, which increases the same trend of silica volume. Consequently, it may slightly reduce sonic slowness in the opposite trend. Therefore, it apparently corroborates porosity and permeability reduction upwards. It is important to highlight that the crossplot confirms the intrusive igneous interval's higher density and lower sonicity compared to the calcareous framework (Ellis and Singer 2010).

P-impedance vs. silica volume

The P-impedance *vs.* silica volume crossplot is a relatively good tool for the characterization of intrusive igneous and silica intervals, presenting a general trend of P-impedance enhancement and silica volume reduction (Figs. 10A, 10B, and 10C). Although the three intervals apparently present a P-impedance overlap, it is possible to observe that interval S3 presents slightly lower values, while interval S1 shows discretely higher values (Fig. 10A). The interval S3 presents a lower silica volume, over 12%, while the interval S2 shows an increase in silica that reaches 20%. Differently, the interval S3 presents a wider spread, which achieves almost 50% of the silica volume. The intrusive interval presents higher P-impedance values and silica content compared to silicified carbonate intervals (Fig. 10A). There is a well-established relationship between P-impedance and permoporosity properties; the lower the P-impedance, the higher the porosity and permeability. Therefore, the intrusive igneous interval is characterized by low permeability and porosity values (Figs. 10B and 10C), and the interval S3 presents the best permoporosity quality, characterized by good to very good values, rarely presenting moderate values. In interval S2, an increase of moderate values is observed, but still good to very good values of porosity and permeability prevail (Figs. 10B and 10C). The interval S1 encompasses mostly moderate porosity values, but permeability seems more compromised than intervals S2 and S3 (Figs. 10B and 10C).

In Well B, a defined trend characterized by P-impedance can be observed through silica intervals (Figs. 10D, 10E, and 10F). From intervals S3 to S1, the P-impedance gradually increases upward, allowing the separation of these intervals in different zones (Fig. 10D). The permoporosity properties appear to display an upward stratification based on their value. The interval S3 presents the best permoporosity values characterized by good to excellent values, rarely presenting moderate values (Figs. 10E and 10F). In the interval S2, an increase of moderate values prevails. In the interval S1, low to moderate values prevail and in less proportion good values (Figs. 10E and 10F). The interval S2 is characterized by intermediate permoporosity values (moderate to good) that also include the lower

interval S3 values and the higher interval S1 values (Figs. 10E and 10F). It is important to highlight that in interval S3, it is possible to identify high silica values that reach over 40% and simultaneously have excellent porosity and very good permeability values (Figs. 10E and 10F).

The use of the crossplot confirms the silica volume increases upward. The increase in P-impedance may be related to the trend of density increase upward once density is used to estimate P-impedance (Penna *et al.* 2019, Castro and Lupinacci 2022). The increase in silica associated with the enhancement of permoporosity in interval S3 for Well B may occur due to the intense dissolution and lack of silica filling locally. This is related to a lower accumulation of silica volume in the lower portion of BVF (Sartorato *et al.* 2020).

DISCUSSION

The intrusion that occurs at Well A is one of the main differences between the studied wells (Figs. 3 and 4). The intrusive bodies observed in the BVF are dated from the Santonian-Campanian age, Upper Cretaceous (Szatmari and Milani 2016, Penna *et al.* 2019, Zhao *et al.* 2019). Chang *et al.* (2008) identified a series of NE-SW rift faults during the Barremian that were reactivated in the Aptian (Lower Cretaceous). For Szatmari and Milani (2016), the faults may have triggered a pathway for hydrothermal fluids during the sedimentation of the Barra Velha Formation. Pinto *et al.* (2017) proposed that hydrothermal fluids were possibly compounded by mantle-derived elements (e.g., Si, Mg, and Ca). These fluids also present CO_2-rich concentrations related to mantle origin through magmatism (Szatmari and Milani 2016, Lima and De Ros 2019, Farias *et al.* 2019, Gamboa *et al.* 2019, Pietzsch *et al.* 2020, Wright 2020). Consequently, the CO_2 degassing by magmatic activity has contributed to increased acidity, favoring carbonate dissolution (Lima and De Ros 2019, Wright and Barnett 2020, De Ros 2021, Carvalho *et al.* 2022). Although Well B is not crossed by any intrusion, it is possible to infer that a nearby one has contributed to hydrothermal fluids, favoring the silicification processes. The well-defined gradual increase of silica has apparently been favored by the intrusion in Well A, and the same process can be correlated for Well B (Figs. 3 and 4).

The best permoporosity values identified in the studied sections are associated with Well B, which presents lower silica volume content and lower GR values. Different authors have pointed out that these characteristics are excellent for carbonate reservoirs, while silica volume increases negatively impact permoporosity (Moore 1989, Ahr 2008, Flügel 2010). Although we observed a decrease in permoporosity properties upwards associated with silica volume increase, some portions of the studied area present a different behavior characterized by silica volume increase and permoporosity enhancement. The different patterns of silica volume content and its impact on other reservoir properties allowed the segmentation of the BVF into three intervals (S3, S2, and S1), and the crossplot analysis led to an understanding of the similarity of intervals between both wells.
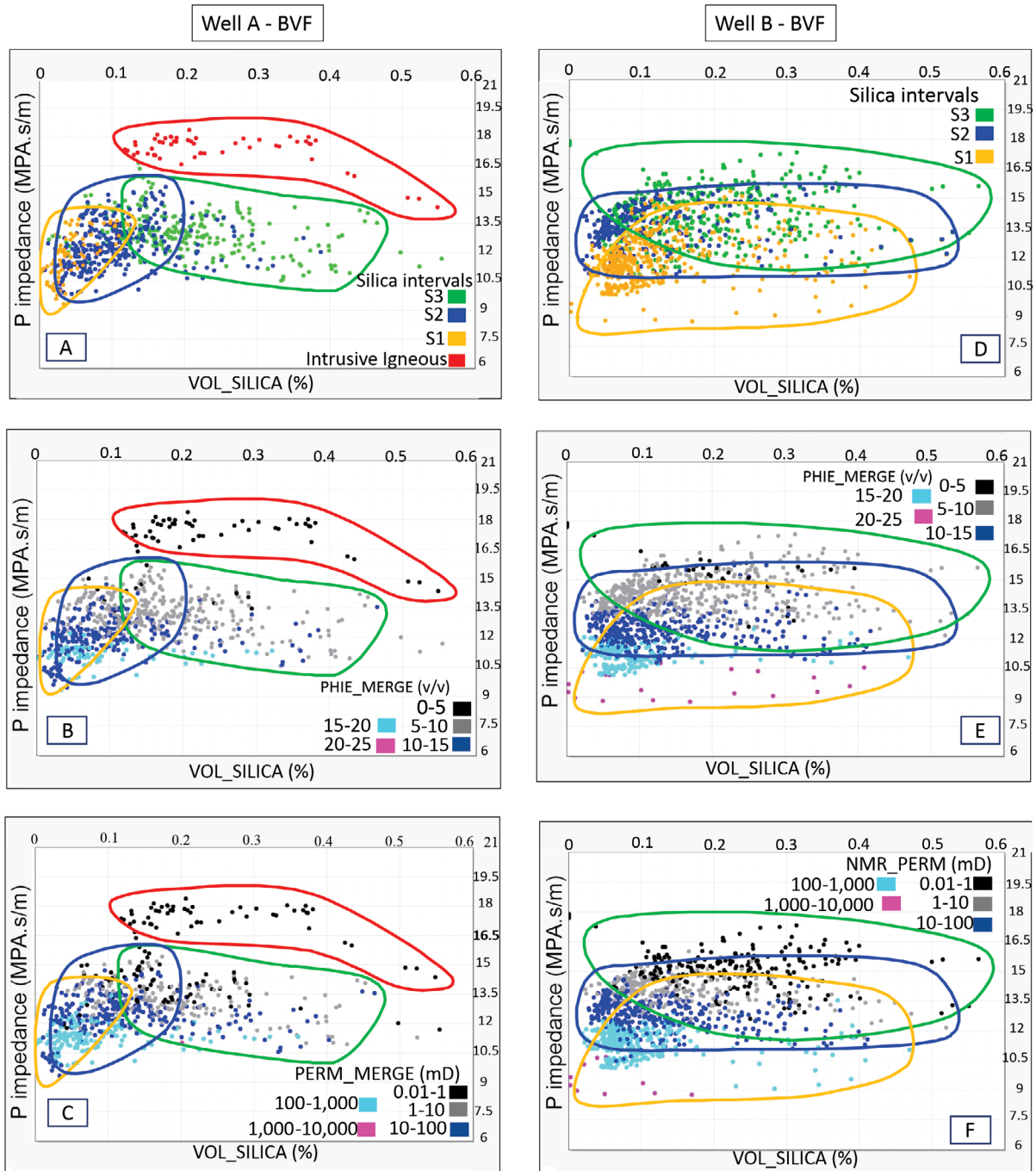
Figure 10. Crossplot of acoustic impedance (P-impedance) *vs.* silica volume (VOL_SILICA) for Wells A and B. (A) Silica and intrusive igneous intervals in Well A. (B) Relationship between the silica intervals, P-IMPEDANCE, VOL_SILICA, and porosity characterization for Well A. (C) Relationship between the silica intervals, P-IMPEDANCE, VOL_SILICA, and permeability characterization for Well A. (D) Silica and intrusive igneous intervals in Well B. (E) Relationship between the silica intervals, P-IMPEDANCE, VOL_SILICA, and porosity characterization for Well B (F) Relationship between the silica intervals, P-IMPEDANCE, VOL_SILICA, and permeability characterization for Well B.

It can be inferred that the permoporosity enhancement associated with silica volume increase could be a product of dissolution and/or fracturing, as observed through BHI analysis (Figs. 5, 6, and 7). The hydrothermal fluids probably became subsaturated with calcite and supersaturated with silica (Bustillo 2010, James and Jones 2016, Lima *et al.* 2020). The calcite subsaturation favored dissolution, followed by silica filling. The dissolution occurred in a higher proportion than silica precipitation, generating porosity enhancement. Sometimes, silicified bedding is fractured, releasing silica intraclasts (Fernández-Ibánez *et al.* 2022) (Fig. 5C). Packard

et al. (2001) built a diagenetic model for the Parkland gas field in Canada in which the hydrothermal CO_2-rich fluids promoted permoporosity enhancement. This dissolution/filling relation is corroborated in the calcite volume *vs.* silica volume crossplot (Fig. 8).

The intrusion compromises reservoir properties, approximately ten meters below the intrusion in Well A (XX24/XX34 m; Fig. 3), due to metamorphism contact aureoles (Anjos and Guimarães 2008, Oliveira *et al.* 2019, Ren *et al.* 2019, Zhao *et al.* 2019). The intrusive rocks have generated a contact metamorphic aureole in surrounding limestones,

characterized by a significant change in the limestone mineral size, rock color, and reservoir pore after marbleization (Ren *et al.* 2019). The reservoir's physical properties decrease after thermal baking.

Herlinger *et al.* (2020) suggested the use of DT *vs.* RHOB crossplot for Mg-clays identification based on the presence of two distinct trends, which indicate different behavior observed in radioactive element-rich clays. In both wells analyses, only one trend was identified (Figs. 9A and 9D). It is possible that the CO_2 increase led to a pH reduction and, consequently, the destabilization of magnesian clays (Farias *et al.* 2019, Wright 2020, Wright and Barnett 2020, De Ros 2021, Carvalho *et al.* 2022). Zones where GR decrease could be associated with nuclear magnetic resonance (NMR) microporosity increase, as were usual in magnesian clays intervals, were not observed.

The P-impedance is important data used in reservoir characterization due to its behavior as a layer property instead of an interface property (Herron and Herron 2000, Sancevero *et al.* 2006). The usage of P-impedance to establish standards even with pre-salt heterogeneity has been demonstrated in different studies (Teixeira *et al.* 2017, Castro and Lupinacci 2019, Dias *et al.* 2021, Ferreira *et al.* 2021, Penna and Lupinacci 2021). Therefore, the P-impedance *vs.* silica volume favors the distinction between the carbonate reservoir and igneous interval and also allows a characterization upwards of the three silica intervals used in this work.

In both wells, an increase in silica volume accumulation was observed. Apparently, due to the lower density of hydrothermal fluids at elevated temperatures (Lima and De Ros 2019, Penna *et al.* 2019, Wright and Barnett 2020), they tend to ascend to the upper portions of the BVF through faults and fractures (Chang *et al.* 2008, Szatmari and Milani 2016, Gamboa *et al.* 2019, Ren *et al.* 2019, De Ros 2021). However, the BVF formation is capped by a thick evaporite layer, the Ariri Formation (Moreira *et al.* 2007, Chang *et al.* 2008). This evaporite layer is characterized by plastic deformation and high thermal conductivity (Mohriak *et al.* 2008). It is possible to infer that the evaporite layer acted as a barrier that favored the hydrothermal fluid's silica-rich accumulation in upper portions of BVF and also contributed to its cooling.

Finally, silicification is an important diagenetic process that played an important role in BVF development. Based on silica accumulation, it was possible to divide the BVF into three segments upward (S3, S2, and S1). It was also possible to establish an opposite trend in permoporosity properties. Interval S3 presents less silica content compared to the other two intervals and the best permoporosity values observed, while interval S1 presents higher silica volume and lower permoporosity properties. The crossplot analysis favors the characterization of reservoir property variations due to silicification impact, allowing different reservoir properties to be quantified.

CONCLUSION

In the studied wells, it is possible to perceive an increase in silica volume from base to top of the Barra Velha Formation associated with a reduction, in a general trend, of porosity and permeability. The laboratory measurements present a very good to excellent correlation to well-log data, corroborating the silica impact on permoporous properties.

The use of acoustic BHI allowed the identification of the alternation of silicified layers and open pore space. The silicified layers showed a good correlation to the high silica volumes obtained through ECS logs. The acoustic BHI, together with ECS, favored the identification of dissolution features that highlighted an anomalous porosity enhancement associated with silica increase. Also, an inversely proportional relationship between silica and calcite volumes was observed both in qualitative and quantitative analyses.

The crossplots related to Well A showed that different reservoir properties allowed good visualization of intrusive igneous intervals and silicified limestones. Moreover, this well-marked characterization of the three silica intervals indicates an increase from bottom to top. Although Well B does not present an igneous interval, the silica content displays the same trend of increase observed in Well A. Probably due to an igneous body being located closer to the well position, favoring the silicification process.

P-impedance *vs.* silica volume crossplot played an important role in reservoir characterization, which allowed us to identify silica increases associated with permoporosity enhancement associated with interval S3. Another advantage observed is the effective characterization of intrusive intervals and calcareous frameworks.

ACKNOWLEDGMENTS

REFERENCES

Ahr W.M. 2008. *Geology of Carbonate Reservoirs:* The identification, description, and characterization of hydrocarbon reservoirs in carbonate rocks. Hoboken: Wiley, 277 p.

Anjos C.W.D., Guimarães E.M. 2008. Metamorfismo de contato nas rochas da Formação Irati (Permiano), norte da Bacia do Paraná. *Revista Brasileira de Geociências*, **38**(4):633-645.

Armenteros I. 2010. Diagenesis of carbonates in continental settings. *Developments in Sedimentology*, **62**:61-151. https://doi.org/10.1016/S0070-4571(09)06202-5

Basso M., Souza J.P.P., Honório B.C.Z., Milani L.H., Chinelatto G.F., Belila A.M.P., Vidal A.C. 2022. Acoustic image log facies and well log petrophysical evaluation of the Barra Velha Formation carbonate reservoir from the Santos Basin, offshore Brazil. *Carbonate and Evaporites*, **37**(3):50. https://doi.org/10.1007/s13146-022-00791-4

Buckley J.D., Bosence D.W., Elders C.F. 2015. Tectonic setting and stratigraphic architecture of an Early Cretaceous lacustrine carbonate platform, Sugar Loaf High, Santos Basin, Brazil. *Geology Society, London, Special Publications*, **418**:175-191. https://doi.org/10.1144/SP418.13

Bustillo M.A. 2010. Silicification of continental carbonates. *Developments in Sedimentology*, **62**:153-178. https://doi.org/10.1016/S0070-4571(09)06203-7

Bustillo M.A., Arribas M.E., Bustillo M. 2002. Dolomitization and silicification in low-energy lacustrine carbonates (Paleogene, Madrid Basin, Spain). *Sedimentary Geology*, **151**(1-2):107-126. https://doi.org/10.1016/S0037-0738(01)00234-2

Butts S.H. 2014. Silicification. *The Paleontology Society*, **20**:15-34. https://doi.org/10.1017/S1089332600002783

Carminatti M., Dias J., Wolf B. 2009. From turbidites to carbonates: breaking paradigms in deep waters. *Offshore Technology Conference*.

Carvalho A.M.A., Hamon Y., De Souza Jr. O.G., Carramal N.G., Collard N. 2022. Facies and diagenesis distribution in an Aptian pre-salt carbonate reservoir of the Santos Basin, offshore Brazil: A comprehensive quantitative approach. *Marine and Petroleum Geology*, **141**:105708. https://doi.org/10.1016/j.marpetgeo.2022.105708

Castro T.M., Lupinacci W.M. 2022. Comparison between conventional and NMR approaches for formation evaluation of presalt interval in the Buzios Field, Santos Basin, Brazil. *Journal of Petroleum Science and Engineering*, **208**(Part D):109679. https://doi.org/10.1016/j.petrol.2021.109679

Castro T.M., Lupinacci W.M. 2019. Evaluation of fine-grains in pre-salt reservoirs. *In*: International Congress of the Brazilian, 16., 2019. *Anais…* Geophysical Society.

Chang H.K., Assine M.L., Corrêa F.S., Tinen J.S., Vidal A.C., Koike L. 2008. Sistemas petrolíferos e modelos de acumulação de hidrocarbonetos na Bacia de Santos. *Revista Brasileira de Geociências*, **38**(2 Suppl.):29-46.

Coates G.R., Xiao L., Prammer M.G. 1999. *NMR logging: principles and applications*. Houston: Haliburton Energy Services. v. 234. 405 p.

De Boever E., Brasier A.T., Foubert A., Kele S. 2017. What do we really know about early diagenesis of non-marine carbonates? *Sedimentary Geology*, **361**:25-51. https://doi.org/10.1016/j.sedgeo.2017.09.011

De Jesus I.L., Lebre M.B.S., Carmo M.C., Fatah T.Y.A., Freire A.F.M., Gamboa L.A.P., Lupinacci W.M. 2021. Analysis of Silica Content and Acoustic Impedance on the Porosity and Permeability in the Barra Velha Formation, Santos Basin. 17th International Congress of the Brazilian Geophysical Society and EXPOGEf.

De Ros L.F. 2021. Syngenetic, Diagenetic and Hydrothermal Processes in the Pre-Salt Sag Section of Santos and Campos Basins. *In*: EAGE Conference on Pre-Salt Reservoir: From Exploration to Production, 2., 2021. *Anais…*

Dias R.M., Lupinacci W.M., Castro T.M., Santos M.A.C. 2021. Understanding the relationship between acoustic impedance and porosity in the presalt of the Buzios Field Santos Basin. *In*: EAGE Workshop on Pre-Salt Reservoir: from Exploration to Production, 2., 2021. *Anais…*

Ellis D.V., Singer J.M. 2010. *Well logging for earth scientists*. Dordrecht: Springer. 692 p.

Farias F., Szatmari P., Bahniuk A., Franca A.B. 2019. Evaporitic carbonates in the pre-salt of Santos Basin–Genesis and tectonic implications. *Marine and Petroleum Geology*, **105**:251-272. https://doi.org/10.1016/j.marpetgeo.2019.04.020

Ferreira D.J.A., Dias R.M., Lupinacci W.M. 2021. Seismic pattern classification integrated with permeability-porosity evaluation for reservoir characterization of presalt carbonates in the Buzios Field, Brazil. *Journal of Petroleum Science and Engineering*, **201**:108441. https://doi.org/10.1016/j.petrol.2021.108441

Fernández-Ibánez F., Jones G.D., Mimoun J.G., Bowen G.M., Simo J.A., Marcon V., Esch W.L. 2022. Excess permeability in the Brazil pre-Salt: Nonmatrix types, concepts, diagnostic indicators, and reservoir implications. *AAPG Bulletin*, **106**(4):701-738. https://doi.org/10.1306/10042120171

Flügel E. 2010. *Microfacies of carbonate rocks:* analysis, interpretation and application. Berlin: Springer. 976 p.

Gaillot P., Brewer T., Pezard P., Yeh E. 2007. *Borehole Imaging Tools: Principles and Applications*. Houston: Copernicus. Scientific Drilling, No. 5.

Gamboa L., Ferraz A., Baptista R., Santos Neto E.V. 2019. Geotectonic controls on CO2 formation and distribution processes in the Brazilian pre-salt basins. *Geosciences*, **9**(6):252. https://doi.org/10.3390/geosciences9060252

Gomes J.P., Bunevich R.B., Tedeschi L.R., Tucker M.E., Whitaker F. 2020. Facies classification and patterns of lacustrine carbonate deposition of the Barra Velha Formation, Santos Basin, Brazilian Pre-salt. *Marine and Petroleum Geology*, **113**:104176. https://doi.org/10.1016/j.marpetgeo.2019.104176

Herlinger R.J., Freitas N.G., Anjos W.D., De Ros L.F. 2020. Petrological and petrophysical implications of magnesian clays in Brazilian Presalt deposits. *In*: SPWLA Annual Logging Symposium, 61, 2020. *Anais…* p. 1-13.

Herlinger R.J., Zambonato E.E., De Ros L.F. 2017. Influence of diagenesis on the quality of lower cretaceous Pre-Salt lacustrine carbonate reservoirs from northern Campos Basin, offshore Brazil. *Journal of Sedimentary Research*, **87**(12):1285-1313. http://dx.doi.org/10.2110/jsr.2017.70

Herron M.M., Herron S.L. 1990. Geological applications of geochemical well logging. *Geological Society, London, Special Publications*, **48**:165-175. https://doi.org/10.1144/GSL.SP.1990.048.01.14

Herron S.L., Herron M.M. 2000. Application of nuclear spectroscopy logs to the derivation of formation matrix density. *In*: SPWLA Annual Logging Symposium, 41, 2000. *Anais…*

Hesse R. 1989. Sílica diagenesis: origin of inorganic and replacement cherts. *Earth-Science Reviews*, **26**(1-3):253-284. https://doi.org/10.1016/0012-8252(89)90024-X

James N., Jones B. 2016. *Origin Of Carbonate Sedimentary Rocks*. United Kingdom: Wiley, 296 p.

Kattah S. 2017. Exploration opportunities in the pre-salt play, Deepwater Campos Basin, Brazil. *Sedimentary Record*, **15**(1):4-8. https://doi.org/10.2110/sedred.2017.1.4

Lai J., Wang G., Wang S., Cao J., Li M., Pang X., Han C., Fan X., Yan L., He Z., Qin Z. 2018. A review on the applications of image logs in structural analysis and sedimentary characterization. *Marine and Petroleum Geology*, **95**:139-166. https://doi.org/10.1016/j.marpetgeo.2018.04.020

Lima B.E.M., De Ros L.F. 2019. Deposition, diagenetic and hydrothermal processes in the Aptian Pre-Salt lacustrine carbonate reservoirs of the northern Campos Basin, offshore Brazil. *Sedimentary Geology*, **383**:55-81. https://doi.org/10.1016/j.sedgeo.2019.01.006

Lima B.E.M., Tedeschi L.R., Pestilho A.L.S., Santos R.V., Vasquez J.C., Guzzo J.V.P., De Ros L.F. 2020. Deep-burial hydrothermal alteration of the Pre-Salt carbonate reservoirs from northern Campos Basin, offshore Brazil: evidence from petrography, fluid inclusions, Sr, C and O isotopes. *Marine and Petroleum Geology*, **113**:104143. https://doi.org/10.1016/j.marpetgeo.2019.104143

Mercedes-Martín R., Ayora C., Tritlla J., Sánchez-Román M. 2019. The hydrochemical evolution of alkaline volcanic lakes: a model to understand the South Atlantic Pre-salt mineral assemblages. *Earth-Science Reviews*, **198**:102938. https://doi.org/10.1016/j.earscirev.2019.102938

Menezes C.P., Bezerra F.H.R., Balsamo F., Mozafari M., Vieira M.M., Srivastava N.K., De Castro D.L. 2019. Hydrothermal silicification along faults affecting carbonate-sandstone units and its impact on reservoir quality, Potiguar Basin, Brazil. *Marine and Petroleum Geology*, **110**:198-217. https://doi.org/10.1016/j.marpetgeo.2019.07.018

Mohriak W., Nemčok M., Enciso G. 2008. South Atlantic divergent margin evolution: rift-border uplift and salt tectonics in the basins of SE Brazil. *Geological Society, London, Special Publications*, **294**:365-398. https://doi.org/10.1144/SP294.19

Moore C.H. 1989. Carbonate diagenesis and porosity. *Developments in Sedimentology*, **46**.

Moreira J.L.P., Madeira C.V., Gil J.A., Machado M.A.P. 2007. Bacia de Santos. *Boletim de Geociências da Petrobras*, **15**:531-549.

Muniz M.C., Bosence D.W.J. 2015. Pre-salt microbialites from the Campos Basin (offshore Brazil): image log facies, facies model and cyclicity in lacustrine carbonates. *Geological Society, London, Special Publications*, **418**(1):221-242. https://doi.org/10.1144/SP418.10

Neves I.D.A., Lupinacci W.M., Ferreira D.J.A., Zambrini J.P.R., Oliveira L.O.A., Olho Azul M., Gamboa L.A.P. 2019. Presalt reservoirs of the Santos Basin: Cyclicity, electrofacies, and tectonic-sedimentary evolution. *Interpretation*, **7**(4):SH33-SH43. https://doi.org/10.1190/INT-2018-0237.1

Oliveira F.V.C.S.R.S., Gomes R.T.M., Silva K.M.S. 2019. Log features for the characterization of igneous rocks in the Pre-Salt area of Santos Basin, SE Brazil. *AAPG International Conference & Exibition*. Argentina.

Packard J.J., Al-aasm I.S., Samson I., Berger Z., Davies J. 2001. A Devonian hydrothermal chert reservoir: The 225 bcf Parkland field, British Columbia, Canada. *American Association of Petroleum Geologists Bulletin*, **85**(1):51-84. https://doi.org/10.1306/8626C75D-173B-11D7-8645000102C1865D

Penna R., Araújo S., Geisslinger A., Sansonowski R., Oliveira L., Rosseto J., Matos M. 2019. Carbonate and igneous rock characterization through reprocessing, FWI imaging, and elastic inversion of a legacy seismic data set in Brazilian pre-salt province. *The Leading Edge*, **38**(1):11-19. https://library.seg.org/doi/full/10.1190/tle38010011.1

Penna R., Lupinacci W.M. 2021. 3D modeling of flow units and petrophysical properties in Brazilian pre-salt carbonate. *Marine and Petroleum Geology*, **124**:104829. https://doi.org/10.1016/j.marpetgeo.2020.104829

Pietzsch R., Tedeschi L.R., Oliveira D.M., Anjos C.W.D., Vazqueza J.C., Figueiredo M.F. 2020. Environmental conditions of deposition of the Lower Cretaceous lacustrine carbonates of the Barra Velha Formation, Santos Basin (Brazil), based on stable carbon and oxygen isotopes: a continental record of pCO2 during the onset of the Oceanic Anoxic Event 1a (OAE 1a) interval? *Chemical Geology*, **535**:119457. https://doi.org/10.1016/j.chemgeo.2019.119457

Pinto V.H.G., Manatschala G., Karpoffa A.M., Ulricha M., Viana A.R. 2017. Seawater storage and element transfer associated with mantle serpentinization in magma-poor rifted margins: a quantitative approach. *Earth and Planetary Science Letters*, **459**:227-237. https://doi.org/10.1016/j.epsl.2016.11.023

Radtke R.J., Lorente M., Adolph B., Berheide M., Fricke S., Grau J., Herron S., Horkowitz J., Jorion B., Madio D., May D., Miles J., Perkins L., Philip O., Roscoe B., Rose D., Stoller C.A. 2012. New Capture and Inelastic Spectroscopy Tool Takes Geochemical Logging to the Next Level. *In*: SPWLA Annual Logging Symposium, 53., 2012, Cartagena, Colombia. *Anais…*

Ren K., Oliveira M.J.R., Zhao J., Zhao J., Oliveira L.C., Rancan C.C., Carmo I.O., Deng Q. 2019. Using Wireline Logging and Thin Sections to Identify Igneous Contact Metamorphism and Hydrothermal Influence on Presalt Limestone Reservoirs in Libra Block, Santos Basin. *In*: Offshore Technical Conference, Brasil. *Anais...*

Sancevero S.S., Remacre A.Z., Portugal R.D.S. 2006. O papel da inversão para a impedância acústica no processo de caracterização sísmica de reservatórios. *Revista Brasileira de Geofísica*, **24**(4):495-512. https://doi.org/10.1590/S0102-261X2006000400004

Sartorato A.C.L., Tonietto S.N., Pereira E. 2020. Silicification and dissolution features in the Brazilian pre-salt Barra Velha formation: Impacts in the reservoir quality and insights for 3D geological modeling: *Rio Oil & Gas*, Rio de Janeiro, Brazil. https://doi.org/10.48072/2525-7579.rog.2020.068

Stanton N., Ponte-Neto C., Bijani R., Masini E., Fontes S., Flexor J.M. 2014. A geophysical view of the Southeastern Brazilian margin at Santos Basin: Insights into rift evolution. *Journal of South American Earth Sciences*, **55**:141-154. https://doi.org/10.1016/j.jsames.2014.07.003

Szatmari P., Milani E.J. 2016. Tectonic control of the oil-rich large igneous-carbonate-salt province of the South Atlantic rift. *Marine and Petroleum Geology*, **77**:567-596. https://doi.org/10.1016/j.marpetgeo.2016.06.004

Teixeira L., Cruz N., Silvany P., Fonseca J. 2017. Quantitative seismic interpretation integrated with well-test analysis in turbidite and presalt reservoirs. *The Leading Edge*, **36**(11):931-937. https://doi.org/10.1190/tle36110931.1

Terra G.J., Spadini A., França A., Sombra C., Zambonato E., Juschaks L., Arienti L., Erthal M., Blauth M., Franco M., Matsuda N., Silva N., Moretti Jr. P., D'ávila R., Souza R., Tonietto S., Anjos S., Campinho V., Winter W. 2010. Classificação de Rochas Carbonáticas Aplicável às Bacias Sedimentares Brasileiras. *Boletim de Geociências Petrobras*.

Tosca N.J., Wright V.P. 2018. Diagenetic pathways linked to labile Mg-clays in lacustrine carbonate reservoirs: a model for the origin of secondary porosity in the cretaceous pre-salt Barra Velha Formation, offshore Brazil. *Geology Society, London, Special Publication*, **435**:33-46. https://doi.org/10.1144/SP435.1

Tucker M.E., Wright V.P. 1990. *Carbonate Sedimentology*. Oxford: Blackwell Scientific Publications. 482 p.

Wright V.P. 2020. The mantle, CO2 and the giant Aptian chemogenic lacustrine carbonate factory of the South Atlantic: Some carbonates are made, not born. *Sedimentology*, **69**(1):47-73. https://doi.org/10.1111/sed.12835

Wright V.P., Barnett A.J. 2015. An abiotic model for the development of textures in some South Atlantic early Cretaceous lacustrine carbonates. *Geological Society, London, Special Publications*, **418**:209-219. https://doi.org/10.1144/SP418.3

Wright V.P., Barnett A.J. 2020. The textural evolution and ghost matrices of the Cretaceous Barra Velha Formation carbonates from the Santos Basin, offshore Brazil. *Facies*, **66**:7. https://doi.org/10.1007/s10347-019-0591-2

Zhao J., Oliveira M.J.R., Zhao J., Ren K., Oliveira L.C., Carmo I.O., Rancan C.C., Deng Q. 2019. Fault activity and its influences on distribution of igneous rocks in Libra block, Santos Basin: Semi-quantitative to quantitative assessment of fault activity based on high-resolution 3D seismic data. *In*: Offshore Technology Conference, Brasil. *Anais…* https://doi.org/10.4043/29691-ms